IMMUNOMETABOLISM

Single-cell NAD(H) levels predict clonal lymphocyte expansion dynamics

Lucien Turner[1], Tran Ngoc Van Le[1]†, Eric Cross[1,2]†, Clemence Queriault[1]†, Montana Knight[1,3], Krittin Trihemasava[1], James Davis[4], Patrick Schaefer[5], Janet Nguyen[1], Jimmy Xu[6], Brian Goldspiel[1], Elise Hall[1], Kelly Rome[1], Michael Scaglione[1], Joel Eggert[7], Byron Au-Yeung[7], Douglas C. Wallace[5,8], Clementina Mesaros[6], Joseph A. Baur[4], Will Bailis[1,2]*

Adaptive immunity requires the expansion of high-affinity lymphocytes from a heterogeneous pool. Whereas current models explain this through signal transduction, we hypothesized that antigen affinity tunes discrete metabolic pathways to license clonal lymphocyte dynamics. Here, we identify nicotinamide adenine dinucleotide (NAD) biosynthesis as a biochemical hub for the T cell receptor affinity–dependent metabolome. Through this central anabolic role, we found that NAD biosynthesis governs a quiescence exit checkpoint, thereby pacing proliferation. Normalizing cellular NAD(H) likewise normalizes proliferation across affinities, and enhancing NAD biosynthesis permits the expansion of lower affinity clones. Furthermore, single-cell differences in NAD(H) could predict division potential for both T and B cells, before the first division, unmixing proliferative heterogeneity. We believe that this supports a broader paradigm in which complex signaling networks converge on metabolic pathways to control single-cell behavior.

INTRODUCTION

Protective adaptive immune responses require the selective expansion of high-affinity antigen-specific lymphocyte clones. The affinity of the antigen receptor (TCR or BCR) to cognate antigen determines the magnitude of the primary response and the rate at which naive lymphocytes exit quiescence (*1*–*3*). During this exit from quiescence, naive lymphocytes reprogram their transcriptome and proteome while, at the same time, remodeling cellular metabolism to meet the demands of rapid proliferation (*3*–*11*). Multiple signaling and transcriptional effectors sensitive to activating signal strength are known to converge on metabolic reprogramming (e.g., Myc, mTOR, and IRF4) (*1*, *2*, *8*, *11*–*29*). Despite this, it remains unclear whether components of the resulting metabolome are similarly sensitive to affinity and work in concert with canonical signaling and gene networks to coordinate the rapid changes in cell cycle biology controlled by antigen receptors.

Here, we test the hypothesis that TCR signaling relays antigen affinity to a discrete set of metabolic pathways responsible for supporting clonal dynamics. Using both unbiased and targeted approaches, we identified nicotinamide adenine dinucleotide (NAD) biosynthesis as a biochemical hub for TCR affinity–driven metabolic remodeling. We find that NAD biosynthesis controls a quiescence exit checkpoint, in which TCR affinity tunes the magnitude of cellular NAD increase and the concurrent rate of cell cycle entry. We demonstrate that whereas mitogenic signaling sets maximal lymphocyte proliferative potential, cellular NAD levels and the biochemistry it facilitates control the rate cells divided within these bounds. Highlighting NAD biosynthesis as a central node for TCR-driven T cell expansion dynamics, we show that normalizing cellular NAD(H) levels is sufficient to normalize proliferation rates between low- and high-affinity ligand–stimulated cells and that enhancing NAD biosynthesis can permit the expansion of lower affinity clones in vivo. Last, we find that this relationship among mitogenic signaling, NAD biosynthesis, and quiescence exit holds true across T and B lymphocytes. Together, these data illustrate how mitogenic signaling converges on cellular metabolism and that regulation of a single, central metabolic process that scales with signal strength ensures that cell cycle demands are met. Accordingly, differences in this one parameter are sufficient to predict how individual lymphocytes behave, both for their metabolic and proliferative capacity. We believe that this provides a broader model for how single-cell metabolic variation drives cellular heterogeneity among populations responding to the same signal.

RESULTS

T cell receptor–ligand affinity coordinates the kinetics of cell cycle progression and anabolic programming in CD8$^+$ T cells

The strength of the activating TCR signal is known to dictate cell cycle entry kinetics and affect differentiation; however, the extent to which metabolic programming is similarly tuned by the TCR remains to be fully elucidated. We used the OT-I TCR transgenic model, in which all T cells encode a TCR with high affinity for the peptide SIINFEKL (N4), with well-defined, lower-affinity variants (e.g., SIIGFEKL, "G4") (*30*–*34*). Consistent with previous findings, the stimulation of OT-I T cells with the higher affinity N4 peptide resulted in more rapid cell cycle entry Myc expression and proliferation compared with the lower affinity G4 peptide (fig. S1, A to E) (*10*, *19*, *33*, *35*–*38*). We then assayed whether the kinetics of downstream

[1]Department of Pathology and Laboratory Medicine, Children's Hospital of Philadelphia, Philadelphia, PA 19104, USA. [2]Department of Pathology and Laboratory Medicine, Perelman School of Medicine, University of Pennsylvania, Philadelphia, PA 19104, USA. [3]Department of Biomedical and Health Informatics, Children's Hospital of Philadelphia, Philadelphia, PA 19104, USA. [4]Department of Physiology and Institute for Diabetes, Obesity, and Metabolism, Perelman School of Medicine, University of Pennsylvania, Philadelphia, PA 19104, USA. [5]Center for Mitochondrial and Epigenomic Medicine, Children's Hospital of Philadelphia, Philadelphia, PA 19104, USA. [6]Center of Excellence in Environmental Toxicology and Department of Systems Pharmacology and Translational Therapeutics, University of Pennsylvania, Philadelphia, PA 19104, USA. [7]Division of Immunology, Lowance Center for Human Immunology, Department of Medicine, Emory University, Atlanta, GA 30322, USA. [8]Department of Pediatrics, Division of Human Genetics, Perelman School of Medicine, University of Pennsylvania, Philadelphia, PA 19104, USA.
*Corresponding author. Email: bailisw@chop.edu
†These authors contributed equally to this work.

metabolic processes were similarly controlled by peptide affinity. At both 24 hours or immediately after stimulation, N4-stimulated cells more rapidly reached higher basal glycolytic and respiration rates than G4-stimulated cells (Fig. 1, A and B). Thus, antigen affinity coordinates cell cycle kinetics with the rate and magnitude of metabolic remodeling.

NAD is a central component of the TCR affinity–dependent metabolome

We next tested whether specific TCR-dependent metabolic pathways underlie this correlation between affinity-driven quiescence exit and T cell metabolic activity. Whereas the global metabolic changes during activation have been characterized, the extent to which specific metabolites are tuned in a scalable, affinity-dependent manner is undefined (*20*, *23*, *39*–*43*). To this end, we performed liquid chromatography–mass spectrometry (LC-MS) on OT-I T cells stimulated for 24 hours with peptides of decreasing affinity—N4, Q4, T4, or G4 (data file S1). We chose this time point because it preceded the first division in all conditions and allowed for optimal capture of metabolic changes associated with quiescence exit (fig. S1, B and F). Principal components analysis revealed that the global metabolite profile was sufficient to distinguish cells on the basis of the affinity, confirming that metabolic rewiring is a central feature of affinity-driven changes during T cell activation (Fig. 1C). Corroborating this, we found that these metabolic signatures were sufficient to predict affinity with a 91.6% prediction accuracy using a random forest analysis (table S1). However, hierarchical clustering revealed that not all metabolites were equally responsive to peptide affinity (Fig. 1D). Whereas some metabolites showed no significant relationship in their response to affinity (clusters 3 and 4), one cluster significantly increased with affinity (cluster 1), and another significantly decreased (cluster 2) (Fig. 1D). We then built a random forest analysis model using specific clusters and found that clusters 1 and 2 predicted affinity with 91.6 and 100% accuracy, respectively (table S1). In contrast, clusters 3 and 4 performed worse compared with the model containing all metabolites (table S1). Thus, a discrete set of metabolites defines affinity-driven T cell biology.

Next, we sought to determine whether any specific metabolites might play a central role in coordinating the TCR affinity–dependent metabolic network and focused our analysis on cluster 1—metabolites that accumulate with increasing affinity. Targeted pathway analysis of cluster 1 found metabolites matched significantly to 14 pathways (table S2). Consistent with TCR affinity's role in proliferation and supporting prior studies, cluster 1 was enriched for metabolites involved in purine synthesis, the citric acid cycle, and the malate-aspartate shuttle (table S2) (*44*). We then ranked metabolites in cluster 1 by the frequency with which they were involved across all identified pathways. This approach revealed that NAD was the most represented metabolite over all significantly enriched pathways (Fig. 1E). We further noted that NMN (a NAD precursor) and metabolites such as orotate and lactate, which require NAD(H) as a coenzyme for their synthesis, were among the most affinity-sensitive metabolites identified (Fig. 1E). Together, these findings led us to hypothesize that NAD functions as a central, affinity-tuned metabolic hub that coordinates the broad biochemical changes of early T cell activation.

TCR signaling tunes the NAD salvage pathway to control single-cell NAD(H) levels

To corroborate our metabolomics findings that TCR affinity controls cellular NAD levels, we used an orthogonal, enzymatic assay to measure NAD. We found that cellular NAD levels are tuned by the strength of TCR stimulation in both a peptide affinity- and concentration-dependent manner (Fig. 1F). This held true when we titrated activating TCR stimuli in P14 transgenic T cells, wild-type (WT) polyclonal mouse $CD8^+$ T cells, and primary human $CD8^+$ T cells, suggesting that this is a generalizable phenomenon (fig. S2, A to C).

To further delineate which signals support the accumulation of cellular NAD, we provided $CD8^+$ T cells with titrated amounts of TCR, CD28, and interleukin-2 (IL-2) stimulation. We found that whereas TCR engagement is absolutely required for enhanced NAD biosynthesis, CD28 stimulation is sufficient to further enhance cellular NAD levels (fig. S2C). Although exogenous IL-2 did not have a discernable impact when cells received high TCR stimulation, we observed that T cell NAD levels were sensitive to IL-2 in G4-stimulated cells, consistent with the role of IL-2 signaling in weakly stimulated T cells (fig. S2, C and D) (*21*).

Because NAD exists in either an oxidized (NAD^+) or reduced (NADH) form, we next investigated whether this activation-induced NAD accumulation was a consequence of redox balance or an absolute increase in NAD. To assay this, we measured NAD and NADH in polyclonal $CD8^+$ T cells activated for 24 hours with a range of anti-CD3ε concentrations. TCR stimulation dose-dependently induced both species, indicating that an absolute increase in total NAD(H) was required (fig. S2E).

NAD is made in cells by three primary pathways: de novo from tryptophan, the Preiss-Handler pathway from nicotinic acid (NA), or the NAD salvage pathway from nicotinamide (NAM) (Fig. 1G) (*45*). We found that only NAD salvage pathway metabolites displayed dose-dependency to TCR stimulation (fig. S2F). Consistent with this and prior reports, inhibition of nicotinamide phosphoribosyltransferase (NAMPT), the rate-limiting enzyme of the NAD salvage pathway with FK866, prevented cellular NAD accumulation after activation (Fig. 1H) (*46*, *47*). To test whether T cells rely solely on the NAD salvage pathway, we attempted to rescue FK866 treatment by supplementing media with tryptophan, NA, or nicotinamide riboside (NR), which bypasses FK866 by supporting NAMPT-independent NMN synthesis (Fig. 1H) (*45*, *48*). Only the salvage pathway precursor NR rescued NAD levels in the presence of FK866 (Fig. 1I). Last, because NAMPT expression is sensitive to T cell activation, we tested whether this is regulated in a signal strength–dependent manner (*47*). Both TCR and costimulation controlled *Nampt* transcript and protein levels (Fig. 1J and fig. S2, G and H). Together, these data support a model in which activating signaling is integrated to promote NAD biosynthesis through the NAD salvage pathway.

Cellular NAD levels are controlled through both biosynthesis and consumption pathways (*45*, *48*). To determine whether TCR signaling similarly tuned NAD consumption, we evaluated NAD decay rates post–FK866 treatment. Across all stimulation conditions, NAD followed a first-order decay kinetic with a half-life of approximately 3.5 hours (fig. S2, I and K). However, because the rate of NAD consumption is a function of concentration as well as half-life, and because NAD concentration increases with affinity, the rate of consumption likewise increases with affinity. In contrast, inhibition of major NAD consumption pathways (PARPs, sirtuins, and CD38) resulted in an increased NAD half-life (fig. S2, J and K). Together, these data suggest that TCR signaling tunes cellular NAD levels through its impact on biosynthesis rather than consumption.

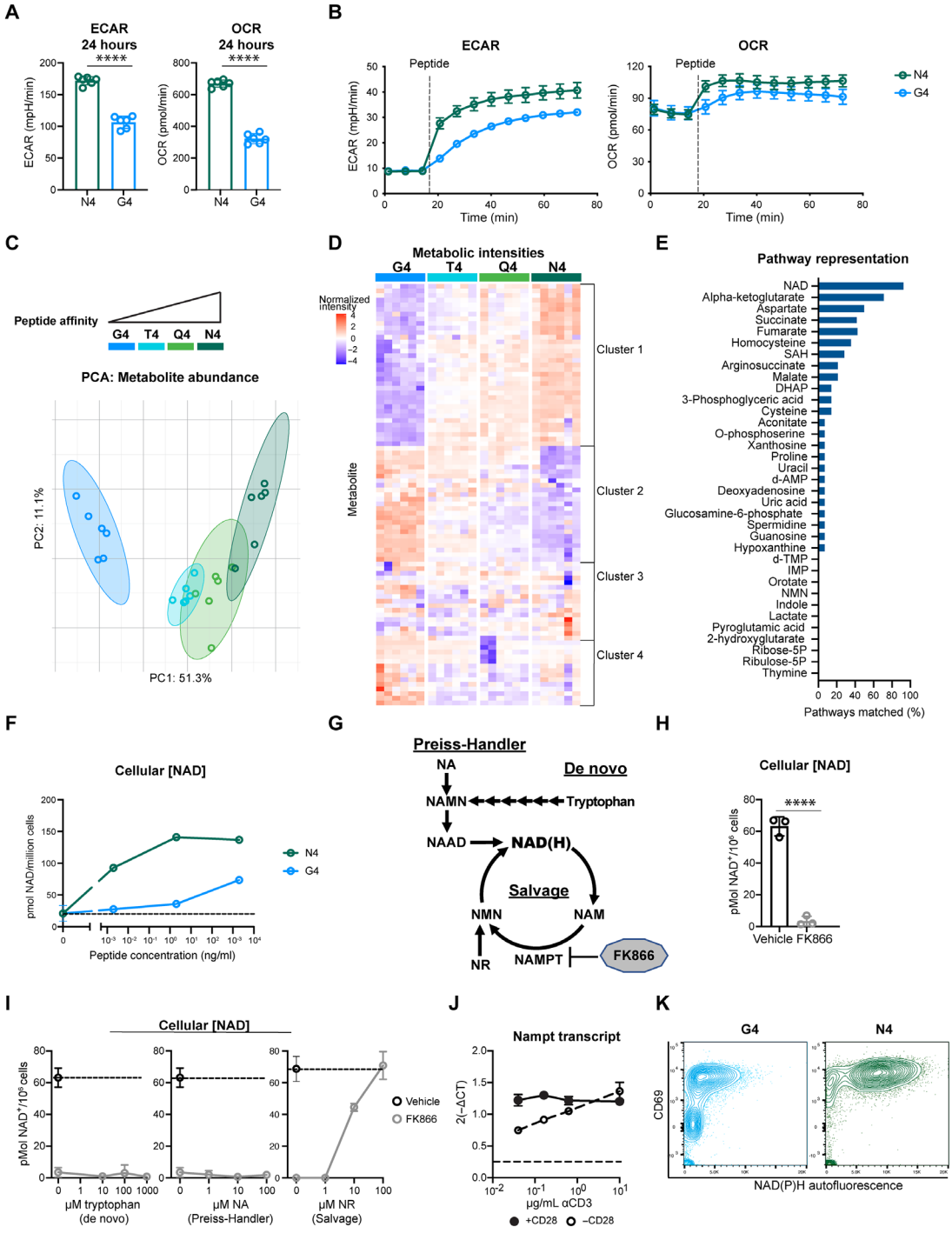

Fig. 1. NAD biosynthesis is a core component of the TCR affinity–dependent metabolome. (**A**) Seahorse analysis of 24-hour peptide-stimulated (G4 or N4) OT-I T cells. (**B**) Seahorse analysis was run on OT-I T cells before and after stimulation with either N4 or G4 peptide (1 μg/ml; added via analyzer port). LC-MS analysis of 24-hour peptide-stimulated (G4, T4, Q4, or N4) OT-I T cells. (**C**) Principal components analysis (PCA) plot generated from metabolite abundance. (**D**) Heatmap of named peaks plotted as $\log_{10}$ fold change of normalized values above G4. (**E**) Pathway analysis using all metabolites in cluster 1. Shown is the percentage of significantly matched pathways corresponding to each metabolite. (**F**) Cellular NAD quantification by cycling assay of OT-I T cells stimulated with N4 or G4 peptide 24 hours after activation. (**G**) Schematic of NAD biosynthesis pathways. (**H**) Cellular NAD quantification by cycling assay in peptide-stimulated OT-I T cells treated with FK866 or vehicle control, 24 hours after activation. (**I**) Cellular NAD quantification by cycling assay in peptide-stimulated OT-I treated with vehicle control or FK866 in the presence of Trp, NA, or NR. (**J**) *Nampt* transcript expression after 24 hours of stimulation with the noted concentrations of anti-CD3ε antibody, with or without anti-CD28 antibody (5 μg/ml). (**K**) Flow cytometry analysis of NAD(P)H autofluorescence and CD69 in peptide-stimulated (G4 or N4) OT-I T cells. Statistical significance was determined using Student's *t* test (A), two-way ANOVA (B) for the interaction of affinity and time in both ECAR and OCR ($P < 0.0001$), (F) of peptide affinity ($P < 0.0001$) and concentration ($P < 0.0001$), (J) for anti-CD3ε levels ($P = 0.0082$) and CD28 stimulation ($P = 0.0007$) was (I) *F* test of nonzero slope Trp ($P = 0.42$), NA ($P = 0.81$), and NR ($P = 0.0005$). ****$P < 0.0001$.

Whereas we observed a direct relationship between TCR signal strength and NAD biosynthesis, the assays described thus far entail bulk analysis, limiting our ability to resolve how TCR-dependent processes such as anabolic state, cell size, and activation status might affect cellular NAD(H). Given that both NAD and NADH changed proportionally in a TCR-dependent manner, we took advantage of the autofluorescent properties of NADH to interrogate single-cell differences in NAD(H) using flow cytometry. Because NADPH has nearly identical autofluorescent properties to NADH, we assayed the specificity and sensitivity of this autofluorescence. The vast majority of NAD(P)H autofluorescence was derived from NAD salvage pathway activity and lost upon FK866 treatment (fig. S3A). We next tested the mitochondrial contribution to the NAD(P)H signature and found that carbonyl cyanide *p*-trifluoromethoxyphenylhydrazone (FCCP) treatment significantly reduced NAD(P)H autofluorescence, but this effect was modest compared with FK866 (fig. S3A). This suggested that whereas the redox state contributes to NAD(P)H autofluorescence, NAD biosynthesis is the dominant source. We next tested whether the per-cell NAD(P)H signal scaled with ligand concentration and/or affinity. NAD(P)H mean fluorescence intensity (MFI) dose-dependently increased with peptide concentrations and affinity, even when controlling for activation status (CD69 expression), size, or Myc expression (Fig. 1K and fig. S3, B and C). Together, these findings indicate that TCR signal strength tunes cellular NAD(H) in an analog manner, independent of activation status, cell size, or the expression of Myc.

Cellular NAD levels pace early cell cycle kinetics to control affinity–driven T cell expansion dynamics

Activated T cells have been shown to be sensitive to pharmacological NAMPT inhibition, and conditional loss of *Nampt* disrupts thymocyte development; however, the requirement for T cell *Nampt* expression during an adaptive immune response is unknown (*46*, *47*, *49*–*53*). To confirm that NAD biosynthesis plays a biologically relevant role in peripheral $CD8^+$ T cell responses, we adoptively transferred either WT or *Nampt*-deficient OT-I T cells into WT recipients and infected those animals with *Listeria monocytogenes*–expressing ovalbumin (Lm-Ova) (fig. S4A) (*50*). Whereas WT OT-I T cells expanded as expected 8 days after infection, *Nampt*-deficient cells failed to do so. Thus, NAD biosynthesis is required for in vivo T cell expansion (Fig. 2A). Suggesting that NAMPT is specifically required in activated T cells, we found an equivalent frequency of circulating OT-I T cells between naive WT and *Nampt*-deficient donors (fig. S4B).

To begin testing our hypothesis that NAD biosynthesis acts as a metabolic conduit for TCR affinity, we asked whether globally enhancing NAD biosynthesis capacity in $CD8^+$ T cells is sufficient to permit expansion of lower affinity clones during a polyclonal response. We therefore bred CD8α-Cre mice to *Nampt* overexpression transgenic animals ($Nampt^{Tg}$) (*54*). $CD8^+$ T cells in these mice express higher basal levels of *Nampt*, uncoupling NAD salvage pathway regulation from TCR affinity (fig. S4C). In $Nampt^{Tg}$ mice infected with Lm-Ova, responding clones displayed a lower normalized SINFEKL-loaded H2-Kb tetramer MFI than WT controls, suggesting that the affinity of the polyclonal response was diminished (Fig. 2B). Despite $Nampt^{Tg}$ animals displaying a lower affinity response, both transgenic and WT mice had the same number of SIINFEKL-reactive T cells, indicating that enhancing NAD biosynthesis is sufficient to permit equitable expansion of lower affinity clones (Fig. 2C).

We next sought to understand the mechanism for how NAD biosynthesis controls the complex cell biology downstream of the TCR. Given that cellular metabolic requirements change throughout T cell differentiation, we asked whether the NAD biosynthesis requirement was restricted to a specific stage of activation (*1*, *2*, *39*, *44*). To this end, we assayed the impact of prolonged inhibition of NAD biosynthesis during or after quiescence exit (Fig. 2D). Cells were most sensitive to NAMPT inhibition before cell cycle entry (days 0 to 2); however, cells rapidly became insensitive to NAD biosynthesis inhibition after quiescence exit (days 2 to 4) (Fig. 2E and fig. S5, A and B). To better resolve these time-dependent requirements, we narrowed our treatment windows to 24 hours (Fig. 2F and fig. S5, C and D). We again observed that cells displayed a heightened sensitivity to FK866 treatment during quiescence exit; however, this sensitivity was lost when most cells had entered the cell cycle (Fig. 2F). Suggesting that this was not simply due to differences in NAD levels over time, NAD levels fell to the limit of detection after FK866 treatment at both ends of the treatment window (days 0 to 1 and 4 to 5) (fig. S5E).

We next asked whether differential metabolic demands before and after quiescence exit explained this temporally restricted requirement for NAD biosynthesis. Using NAD(P)H fluorescence lifetime imaging microscopy (FLIM), we were able to attain information about the free (shorter lifetime) and protein-bound (longer lifetime) ratio of NAD(P)H in the cell. Loss of NAD biosynthesis had a greater impact on fluorescence lifetime in early activated T cells than later stage cells, indicating that recently activated T cells have a heightened requirement for NAD biosynthesis to maintain proper NAD(H) utilization throughout the cell (Fig. 2G).

Because NAD is a coenzyme both for mitochondrial respiration and glycolysis, we tested whether these two processes were differentially sensitive to NAD salvage pathway inhibition at the time of activation and shortly after. Days 0 to 1 of FK866 treatment resulted in a marked impairment of glycolysis (Fig. 2H and fig. S5F). In stark contrast, days 1 to 2 of FK866 treatment yielded no detectable differences in glycolytic rate. Similarly, days 0 to 1 of FK866 treatment almost completely abrogated mitochondrial respiration, whereas basal OCR was marginally affected after days 1 to 2 of FK866 treatment, with spare respiratory capacity showing some sensitivity (Fig. 2H and fig. S5, G and H). These data suggest that T cells have a heightened requirement for NAD biosynthesis to support glycolysis and mitochondrial respiration as they enter the cell cycle, which is lost shortly after.

Our data demonstrate that the magnitude of TCR signaling generates a commensurate NAD biosynthesis response that is required as T cells exit quiescence. We therefore asked whether the degree of NAD biosynthesis downstream of a given TCR affinity directly regulated cell cycle rates in those cells. In the presence of FK866, NAM cannot be recycled back to NMN, leaving NMN synthesis reliant on the amount of NR supplemented in the medium and enabling tight control of NAD biosynthesis capacity (Fig. 1G and fig. S6A). For both N4 and G4 peptides, T cell expansion was proportionately controlled by the concentration of NR in the culture (fig. S6B). Whereas we also observed that NAD biosynthesis capacity controlled T cell viability over time, there was no effect on cell survival within the first 24 hours (fig. S6C). This permitted us to assess the interaction of NAD with the cell cycle within this window. We found that NAD biosynthesis

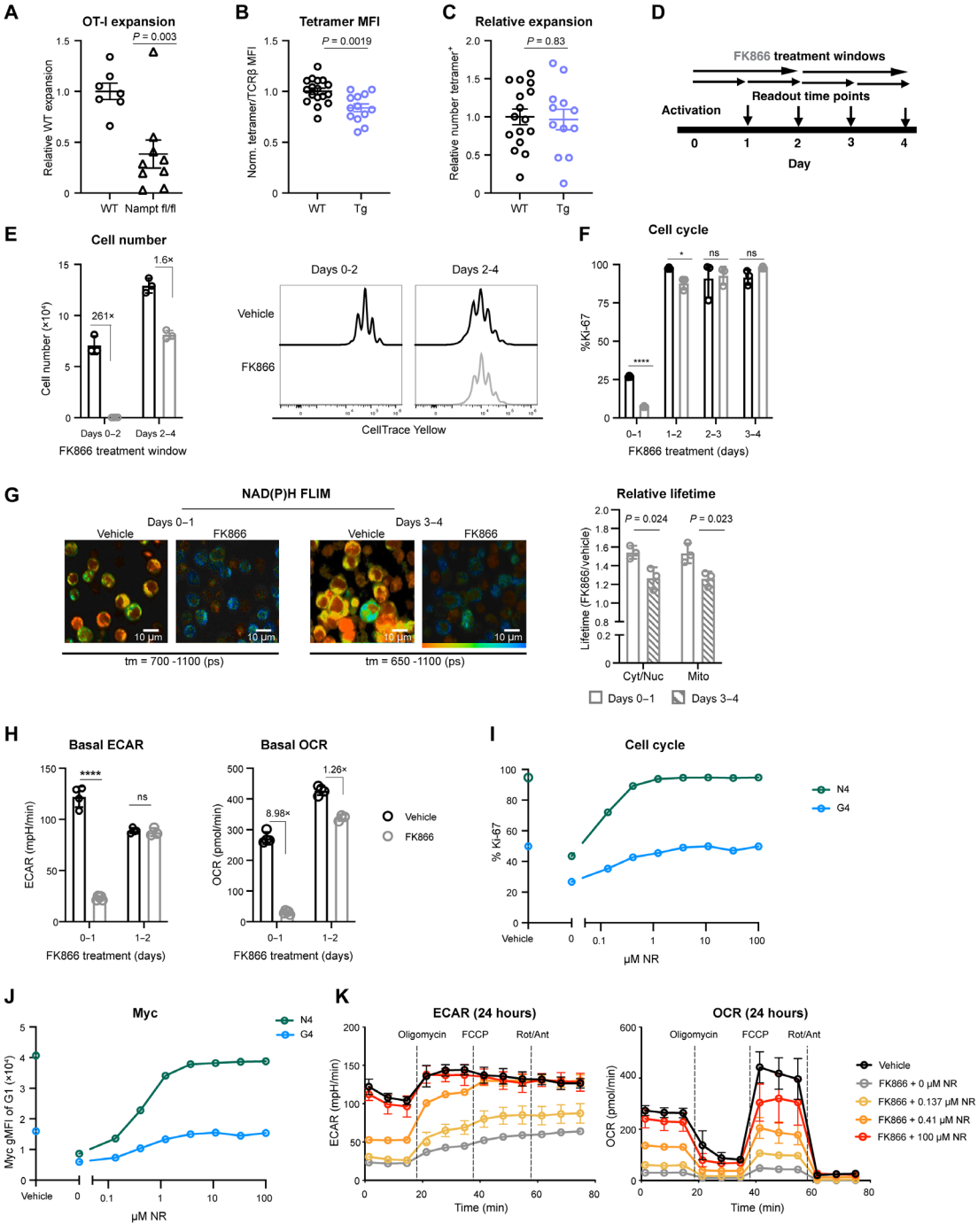

Fig. 2. Cellular NAD levels control affinity–driven T cell expansion dynamics. (**A**) CD8$^+$ T cells from Nampt$^{fl/fl}$ × CD8α-Cre × OT-I mice or Cre controls were transferred into Lm-Ova–infected CD45.1 recipients. The relative number of transferred cells was quantified on day 7 after infection. WT or Nampt Tg × CD8α-Cre mice were infected with Lm-Ova and analyzed on day 7 after infection. (**B**) Quantification of SIINFEKL-H2-Kb tetramer gMFI, normalized to TCRβ gMFI. (**C**) The number of SIINFEKL-H2-Kb tetramer$^+$ cells. (**D**) Schematic of experimental design for (**E**) to (**I**). CD8$^+$ T cells were activated and treated with FK866 or vehicle control for 24 or 48 hours from the indicated time points. (E) Cell number and proliferation (48-hour treatment windows). (F) Cell cycle entry (24-hour treatment windows). CD8$^+$ T cells were activated and treated with FK866 or vehicle control from either days 0 to 1 or 3 to 4. (G) NAD(P)H fluorescence lifetime in the mitochondria and cytoplasmic/nuclear compartments, plotting relative lifetime in FK866 versus vehicle controls. (H) Basal ECAR and OCR in activated CD8$^+$ T cells treated with FK866 or vehicle control from days 0 to 1 or 1 to 2. Peptide-stimulated (N4 or G4) OT-I T cells were treated with FK866 ± NR at the indicated concentration. After 24 hours, (I) the frequency of Ki67$^+$ cells and (**J**) Myc gMFI in G1 cells was quantified. (**K**) Seahorse Mito Stress Test of WT CD8$^+$ T cells treated with FK866 and NR at the indicated concentrations, 24 hours after stimulation. Results from two (A) or three (B) independent experiments are shown. Statistical significance was calculated in (A) to (C) and (E) to (G) using multiple unpaired *t* tests using a two-stage step-up (Benjamini, Krieger, and Yekutieli). (H) Multiple comparisons *t* test using Holm-Šidák correction was used for ECAR. Student's *t* test of fold change for OCR. EC_{50} calculated for (I): N4 = 0.093 μM NR, G4 = 0.197 μM NR and (J) N4 = 0.42 μM NR, G4 = 0.43 μM NR. *$P \leq 0.05$. ****$P < 0.0001$. ns, not significant.

capacity sets the kinetics of G1 entry, G2 progression, and the time to the first division downstream of a given TCR signal strength (Fig. 2I and fig. S6, D to F). Furthermore, high- and low-affinity–stimulated T cells displayed differential sensitivity to NAD biosynthesis capacity over time. Whereas N4- and G4-stimulated cells exhibited similar NAD dependencies at the time of cell cycle entry, N4-stimulated cells displayed an increasing requirement for expansion later (Fig. 2, I and J, and fig. S6, B and G). Combined, these data demonstrate that NAD biosynthesis capacity dictates the rate of quiescence exit and cell cycle progression to control expansion dynamics in activated T cells, within the bounds set by the corresponding strength of signaling.

Because T cell quiescence exit is controlled by mTOR signaling and Myc expression, we asked whether NAD biosynthesis might modulate these key anabolic regulators. We observed that the phosphorylation of the mTOR substrate S6 and the kinetics of and amplitude of Myc expression were dose-dependently sensitive to NR supplementation, suggesting that NAD biosynthesis capacity is limiting for both factors (Fig. 2J and fig. S6H). We next tested whether cellular NAD levels also control T cell metabolic capacity. NAD biosynthesis capacity dose-dependently controlled the rates of both glycolysis and mitochondrial respiration (Fig. 2K).

NAD biosynthesis governs a quiescence exit checkpoint in activated CD8$^+$ T cells

We next asked whether the cell cycle arrest exhibited after NAD salvage pathway inhibition represents a reversible checkpoint-like phenomenon or an irreversible process such as senescence and/or cell death. We thus assayed whether cells unable to undergo NAD biosynthesis at the time of activation could be rescued and enter the cell cycle if the NAD salvage pathway was restored in a delayed manner (Fig. 3A and fig. S7A). No differences in T cell viability and activation before NR supplementation were observed in FK866-treated compared to vehicle-treated cells (figs. S6C and S7, B and C). Delayed NR supplementation resulted in a rapid recovery of G1 entry, with the frequency of G1 cells returning to that of untreated controls (Fig. 3B). After this initial NR treatment period, "rescued" cells were then able to successfully proliferate, with nearly 100% of cells dividing 24 hours later (fig. S7D). These data indicate that NAD biosynthesis is necessary and sufficient for activated T cell quiescence exit and that the cell cycle arrest observed upon NAD salvage pathway inhibition is reversible.

Using this delayed NAD rescue approach, we tested whether the cell cycle kinetics set by a given TCR affinity were dependent on the corresponding magnitude of NAD biosynthesis generated downstream. G4-stimulated cells were similarly able to exit quiescence and elevate Myc protein expression, however, with a less rapid recovery kinetic than N4-stimulated cells (Fig. 3, C to E). Consistent with NAD biosynthesis being a rate-limiting factor for affinity-dependent cell cycle differences, limiting NAD biosynthesis capacity in N4-stimulated cells slowed cell cycle entry and Myc protein expression to rates comparable to those in G4-stimulated cells (Fig. 3, C to E).

T cell quiescence exit is known to require mTOR activity (*21*, *24*, *25*). We thus asked whether mTOR signaling was likewise essential for the NAD-dependent checkpoint. Like cell cycle entry and Myc expression, S6 and S6K phosphorylation were quickly restored after delayed NAD rescue, suggesting that NAD biosynthesis is also necessary and sufficient for mTOR signaling during quiescence exit (fig. S7, E and F). Conversely, Torin treatment minimally affected the rate of G1 entry after delayed NAD rescue while only partially abrogating Myc protein expression (fig. S7, G to I). Consequently, whereas mTOR signaling is required for optimal proliferation and Myc expression, re-engagement of mTOR activity does not fully explain how NAD biosynthesis controls quiescence exit.

We next hypothesized that once activation has occurred, NAD might regulate quiescence exit independent of mitogenic signaling. We thus asked whether NAD-dependent quiescence exit required sustained TCR and costimulatory signaling (fig. S7J). Regardless of whether T cells received continuous stimulation or were removed before rescue, we observed that NR supplementation restored proliferative capacity and Myc expression to comparable levels (fig. S7, K to M). These data demonstrate that mitogenic signals poise T cells for cell cycle entry and dictate the maximal rate of this response; however, quiescence exit cannot occur until T cells overcome a NAD biosynthesis–dependent checkpoint.

NAD biosynthesis governs the rates of glycolysis and respiration to control quiescence exit

The coincidence of a NAD requirement for quiescence exit and sustaining energetics during early T cell activation led us to hypothesize that these two processes were connected. Metabolic processes including glycolysis, the citric acid cycle, and oxidative phosphorylation are known to regulate cell cycle progression in T cells (*1*, *2*, *39*, *44*). Having seen that glycolysis and mitochondrial respiration require the NAD salvage pathway during early activation, we first tested whether T cells engage these metabolic processes during the delayed NAD rescue assay. We observed dose-dependent increases in basal and maximum extracellular acidification rate (ECAR) and oxygen consumption rate (OCR) after NR supplementation (Fig. 3F and fig. S8A).

Because NAD(H) regulates many biochemical pathways beyond glycolysis and respiration, we aimed to globally characterize the NAD(H)-dependent pathways engaged during T cell quiescence exit. To do so, we performed mass spectrometry on OT-I T cells at 0, 30, 120, and 240 min after delayed NR treatment. Validating this approach, we saw that FK866 resulted in a notable depletion of cellular NAD levels that rapidly increased after NR supplementation (fig. S8B). In turn, this loss and recovery of cellular NAD had broad and differential effects on amino acids, nucleic acids, and central carbon metabolism (fig. S8B). A majority (63%) of all detected metabolites displayed significant sensitivity to the NAD salvage pathway, indicating that NAD biosynthesis plays a critical role in maintaining the metabolic landscape during quiescence exit (Fig. 3G).

Among the most notable NAD-dependent changes, we observed that glycolysis was markedly sensitive during the delayed NAD rescue assay (Fig. 3H). FK866 treatment resulted in a buildup of metabolites in glycolysis upstream of the glyceraldehyde-3-phosphate dehydrogenase (GAPDH) step and a depletion of metabolites immediately downstream. Reciprocally, this block was reversed after NR supplementation (Fig. 3H). These data suggest that NAD biosynthesis is required to support the rapid increase in glycolysis during early T cell activation via GAPDH. Whereas GADPH reduces NAD to NADH, the NADH-oxidizing activity by LDH is understood to help recover NAD in highly glycolytic cells, where free NAD can become rate limiting. We observed that FK866 treatment had minimal effects on lactate and pyruvate levels but that lactate quickly accumulated after NR supplementation with pyruvate trending down over time,

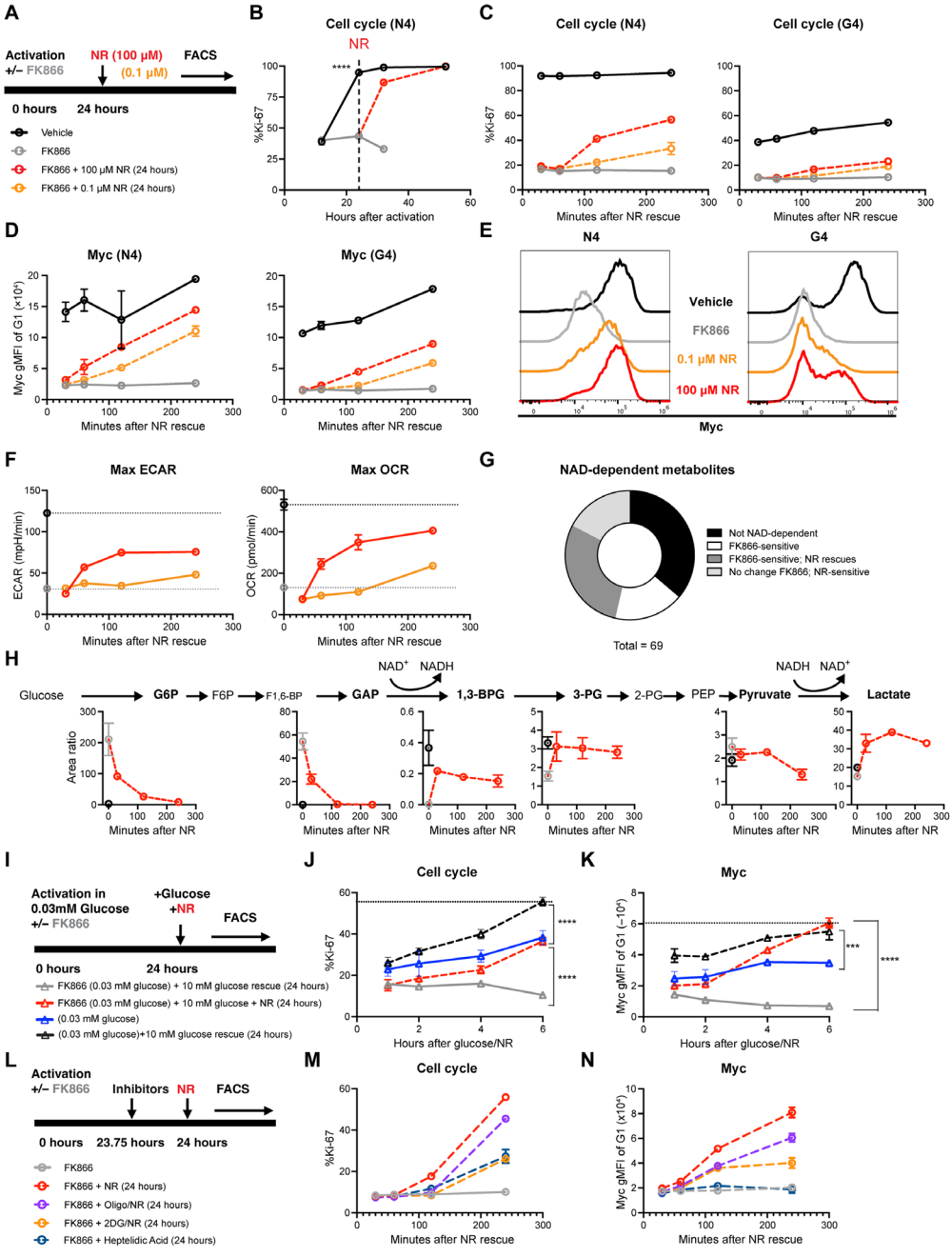

Fig. 3. NAD biosynthesis governs a quiescence exit checkpoint. (**A**) Schematic of "delayed NAD rescue" assay. (**B**) Peptide-stimulated OT-I T cells were with FK866 for 24 hours and then acutely supplemented with 100 μM NR (hereafter, the "delayed NAD rescue assay"). The frequency of Ki-67$^+$ cells was quantified at the indicated time points post–NR treatment. After 0.1 or 100 μM NR treatment of peptide-stimulated (N4 or G4) OT-I T cells during the delayed NAD rescue assay, (**C**) the frequency of Ki67$^+$ cells and (**D**) Myc gMFI in G1 cells was quantified. (**E**) Representative plots of Myc protein expression at 4 hours after NR supplementation. (**F**) Seahorse Mito Stress Test on OT-I T cells after delayed NAD rescue assay, with maximal ECAR and OCR plotted. Untargeted LC-MS was performed on cells subjected to the delayed NAD rescue assay to quantify relative metabolite abundance pre– and post–NR supplementation (30, 60, 240 min). Peak areas were normalized to an internal standard. (**G**) Frequency of all detected metabolites that were NAD sensitive. (**H**) Schematic of glycolysis shown above graphs plotting the abundance of the bolded metabolites during the delayed NAD rescue assay. (**I**) Experimental schematic for (**J**) and (**K**). The delayed NAD rescue assay was performed on OT-I T cells in either control medium or medium containing 0.03 mM glucose. After 24 hours, cultures were supplemented with NR, limiting glucose cultures were supplemented with 10 mM glucose, and (J) cell cycle entry and (K) Myc gMFI in G1 cells were quantified. The dotted line denotes vehicle control levels at the time of NR addition. (**L**) Experimental schematic of (**M**) and (**N**). The delayed NAD rescue assay was performed on OT-I T cells treated with the indicated inhibitors 10 min before NR supplementation, and (M) the frequency of Ki-67$^+$ cells and (N) Myc gMFI in G1 cells was quantified. Significance was calculated using (B) multiple unpaired *t* tests with two-stage step-up (Benjamini, Krieger, and Yekutieli) and (C and D) *F* test comparing the slope of linear regression between 100 and 0.1 μM NR conditions. (F) Two-way ANOVA for dose and time interaction for max ECAR and max OCR. (G, M, and N) Multiple comparisons using Tukey's correction. (J and K) Šidák's multiple comparisons. All comparisons are significant except (M) 2DG and HA as well as (N) HA and FK866. ****$P < 0.0001$.

confirming that glycolysis is rapidly engaged after NAD biosynthesis is restored (Fig. 3H). Our findings suggest that NAD(H) levels are limiting in early T cell activation and that NAD biosynthesis is required to sustain the high rate of GAPDH activity in these cells. Whereas LDH activity may help recover free NAD to support this high glycolytic rate, it cannot restore redox balance sufficient for GAPDH in the absence of the NAD salvage pathway.

These findings led us to hypothesize that affinity-dependent NAD biosynthesis controls quiescence exit kinetics through its regulation of the rate of glycolysis and respiration. We first evaluated the impact glucose restriction has on cell cycle entry during T cell activation (fig. S8, C and D). We asked whether delayed glucose supplementation could rescue quiescence exit in those conditions and in turn whether NAD biosynthesis governs the rate at which this occurs (Fig. 3I). We then tracked cell cycle entry over the following 6 hours (Fig. 3J). Whereas delayed glucose supplementation permitted cell cycle entry and restored Myc levels, this was entirely dependent on the NAD biosynthesis capacity of the cells (Fig. 3, J and K). Thus, whereas glucose availability is necessary for cell cycle entry, it alone is not sufficient, because NAD biosynthesis is required for glucose utilization during quiescence exit.

Because NAD(H) has roles beyond its activity as a coenzyme, we next sought to test the alternative hypothesis that rather than acting through central carbon metabolism, NAD biosynthesis primarily supports quiescence exit through its role as a substrate for NAD-consuming enzymes (i.e., sirtuins, PARPs, and CD38) (*45*, *48*). Whereas inhibitory drugs against these pathways were sufficient to extend the NAD consumption half-life, they did not abrogate cell cycle entry after NR rescue (figs. S2J and S8E). We repeated this assay by treating cells with 2-deoxy-D-glucose (2DG), oligomycin, or heptelidic acid (HA) to inhibit glycolysis, adenosine 5′-triphosphate synthase, or GAPDH, respectively. All three inhibitors were sufficient to blunt cell cycle entry, with 2DG and HA exhibiting the most potent effects (Fig. 3M). Similar to our cell cycle entry results, 2DG, oligomycin, and HA all abrogated Myc protein expression after NR supplementation, with inhibition of glycolysis and GAPDH resulting in the most robust reduction in Myc protein expression (Fig. 3N).

These data indicate that NAD biosynthesis licenses cells to exit quiescence through its role as a rate-limiting factor in central carbon metabolism. Once cells have cleared this checkpoint and entered the cell cycle, their reliance on NAD biosynthesis starkly decreases, highlighting the distinct biochemical requirements at the time of cell cycle entry. Together, our findings support a model during early T cell activation in which sufficient carbon source availability and NAD biosynthesis are together required for quiescence exit to facilitate the energetic and synthetic demands of division. Given that the magnitude of NAD biosynthesis is proportional to ligand affinity, NAD functions as a metabolic conduit for TCR signal strength in controlling T cell expansion dynamics.

Single-cell differences in NAD(H) underlie heterogeneity in lymphocyte proliferative responses

Thus far, our findings illustrate how TCR signal strength tunes cellular NAD levels in T cells to license the biochemical remodeling required for quiescence exit. Whereas this was found at the population level, our NAD(P)H flow cytometry results show a broad distribution in NAD(H) levels among individual T cells responding to the same stimuli. Given that proliferation rates are not uniform across populations of identically stimulated T cells, we hypothesized that single-cell differences in NAD(H) underlie this heterogeneity. We first asked whether the NAD(H) heterogeneity observed was a readout for population-level heterogeneity in TCR engagement or metabolic heterogeneity in cells receiving comparable signals. Because Nur-77 expression is a highly sensitive reporter of TCR signal strength, we used OT-I × Nur77-GFP mice to permit simultaneous assessment of single-cell differences in TCR signaling and NAD(P)H autofluorescence. As expected, Nur77-GFP expression was dependent on TCR affinity and antigen concentration (fig. S9A). We observed heterogeneity in the NAD(P)H signal even within populations of comparable Nur77-GFP expression (fig. S9B). These data suggest that whereas the median NAD biosynthesis capacity in a population of T cells scales with the strength of TCR stimulation, there exists a wide range of metabolic heterogeneity among individual cells, above and below this median.

To further test whether variation in single-cell NAD(H) levels contributes to activated T cell heterogeneity, we developed a flow cytometry sorting strategy that enabled us to unmix populations of cells based on NAD(P)H and then return them to culture. Using this approach, we ensured that all sorted cells were activated ($CD69^+$) and had not undergone their first cell division (CTY) (Fig. 4A). Consistent with our findings that NAD levels support T cell metabolic potential, $NAD(P)H^{high}$ cells exhibited higher rates of glycolysis and oxygen consumption 24 hours after sort (Fig. 4B). In addition, we found that the magnitude of early cellular NAD(P)H was predictive of the rate that T cells exited quiescence and progressed through the cell cycle as early as 12 hours after sort (Fig. 4C). Looking 24 hours after sort, initial cellular NAD(P)H levels predicted that both the rate T cells underwent their first division and their early proliferative potential, with the number of divisions proportional to NAD(P)H levels at the time of sort (Fig. 4D).

We next asked whether differences in single-cell NAD(P)H could help explain the differences in proliferative potential between high- and low-affinity ligand–stimulated cells and whether normalizing NAD(P)H autofluorescence between low- and high-affinity cells would be sufficient to normalize responses (Fig. 4E). As expected, unsorted N4-stimulated OT-I T cells proliferated to a much greater extent than G4-stimulated cells (Fig. 4F). In contrast, when cellular NAD(P)H levels were normalized across activating conditions, G4-stimulated cells were capable of proliferating nearly to the same extent as N4-stimulated cells. Whereas N4-stimulated cells retained a slight advantage after sorting, NAD(P)H levels explained 94% of the variance in proliferation across sorted populations (Fig. 4F). Furthermore, pre-division differences in single-cell NAD(P)H were deterministic of proliferative dynamics in naive T cells, T cells stimulated with peptides of intermediate affinities, and when controlling for fluctuations in NAD(P)H autofluorescence by concurrently sorting high- and low-affinity stimulated cells (fig. S9, C and D). Together, our data indicate that T cell activation generates a continuum of single-cell NAD(H) levels, with increasing ligand affinity resulting in a broader distribution and a higher median. Whereas low- and high-affinity stimulated T cells are phenotypically distinct at the population level, initial differences in single-cell NAD(P)H are sufficient to explain heterogeneity in proliferative potential across ligand affinities.

Because effector function acquisition is tightly coupled to proliferative capacity, we next asked whether pre-division NAD(P)H was also predictive of cytokine production. Consistent with cell division kinetics, initial NAD(P)H levels predicted future functional capacity,

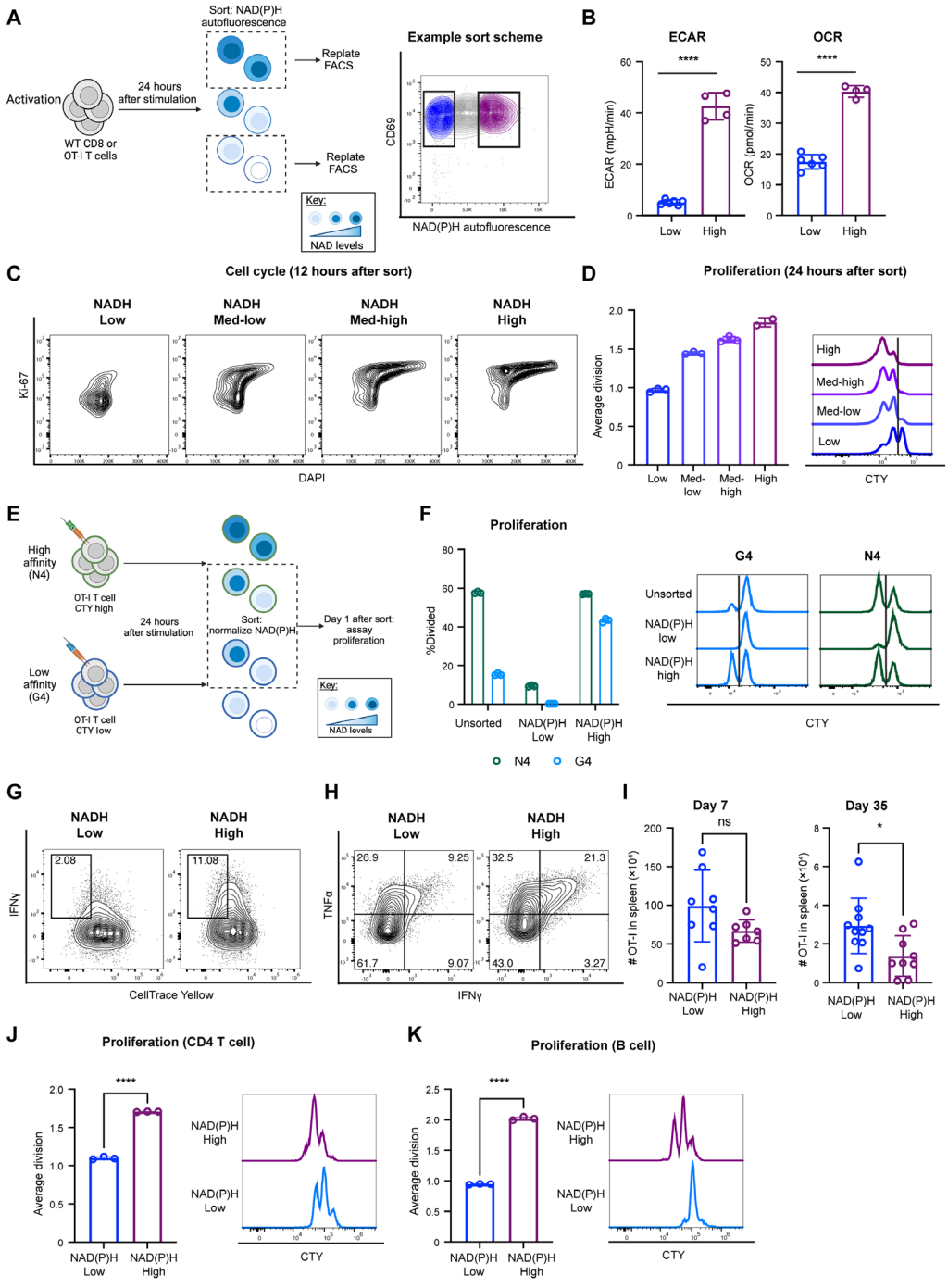

Fig. 4. Single-cell differences in NAD(H) underlie lymphocyte heterogeneity. OT-I T cells were stimulated with peptide for 24 hours, and then CD8$^+$ CD69$^+$ cells were sorted by NAD(P)H autofluorescence. (**A**) Experimental schematic and example gating strategy. (**B**) Basal ECAR and OCR of NAD(P)H-high and -low cells 1 day after sort. N4-stimulated OT-I T cells were sorted by quartiles of NAD(P)H autofluorescence and evaluated for (**C**) cell cycle 12 hours after sort or (**D**) proliferative capacity 24 hours after sort. (**E**) Schematic of NAD(P)H normalization sorting strategy. (**F**) OT-I T cells were stimulated with N4 or G4 peptide for 24 hours and were then sorted using the same gates for NAD(P)H-high and -low cells. Shown is the frequency of divided cells in each population, 24 hours after sort. WT CD8$^+$ T cells were stimulated and sorted by NAD(P)H autofluorescence at ~20 hours after stimulation. Three days after sort, cells were restimulated and evaluated for (**G**) proliferation (CTY) and IFN-γ production and (**H**) TNF-α and IFN-γ. (**I**) After 24 hours, N4-stimulated 45.1 OT-I T cells were sorted by NAD(P)H and adoptively transferred into Lm-Ova–infected, congenically marked recipients on day 1 after infection. At days 7 and 35, the number of transferred splenic OT-I T cells was quantified. WT CD4$^+$ T cells or B cells were stimulated with anti-CD3ε and anti-CD28 plate-bound antibodies or LPS, respectively. Cells were sorted 20 hours after stimulation on the basis of NAD(P)H autofluorescence. Proliferation was determined 1 day after sort for (**J**) CD4$^+$ T cells and (**K**) B cells. Statistical significance was determined using (B, I, J, and K) Student's *t* test, (D) *F* test of nonzero slope of the linear regression of the rank assigned data, and (F) two-way ANOVA, which determined that NAD(P)H levels contributed to 93.8% of the variance in sorted conditions. $*P < 0.05$ and $****P < 0.0001$.

with NAD(P)H^{high} cells producing more interferon-γ (IFN-γ) and tumor necrosis factor–α (TNF-α) (Fig. 4, G and H, and fig. S9E). Moreover, NAD(P)H^{high}-sorted cells displayed greater overall polyfunctionality compared with NAD(P)H ^{low} cells (fig. S9F). Thus, early differences in single-cell metabolism are deterministic of the proliferative dynamics from a population of activated cells. This metabolic feature can further be used to isolate cells with discrete characteristics from an otherwise heterogeneous pool.

The characteristics we observed in NAD(P)H^{high} cells (rapid proliferation, high glycolytic engagement, and early acquisition of effector function) were consistent with the major hallmarks of early effector cells, which quickly expand but poorly persist in vivo. We therefore asked whether early differences in single-cell NAD(P)H levels were similarly deterministic of in vivo T cell dynamics. We activated OT-I T cells with N4 peptide, sorted NAD(P)H^{high} and NAD(P)H^{low} cells, and adoptively transferred them into congenically marked recipients that had been infected with Lm-Ova 1 day before transfer. We found that whereas NAD(P)H^{high} and NAD(P)H^{low} cells expanded to equivalent levels at day 7 after infection, NAD(P)H^{high} cells contracted to a greater extent by day 35 after infection compared with NAD(P)H^{low} cells (Fig. 4I and fig. S9G). Together with our in vitro findings, these data suggest that metabolic heterogeneity before the first division is not only deterministic of early expansion dynamics but also long-term persistence in vivo.

Antigen receptor-ligand affinity control of cell expansion dynamics is not unique to CD8$^+$ T cells but is a shared feature with CD4$^+$ T cells and B lymphocytes. We therefore asked whether the relationship we observed between CD8$^+$ T cell ligand affinity, NAD biosynthesis, and cell cycle kinetics was conserved in these other lymphocyte populations. Like CD8$^+$ T cells, antigen receptor signaling drove a dose-dependent increase of cellular NAD in both CD4$^+$ T and B cells (fig. S10, A and D). As with BCR stimulation, increasing TLR stimulation drove a dose-dependent increase in cellular NAD, suggesting that NAD biosynthesis plays a role in response to a broad range of mitogenic signals (fig. S10E). FK866 treatment abrogated G1 entry and Myc expression in CD4$^+$ T and B cells, suggesting that NAD biosynthesis is a general requirement for lymphocyte quiescence exit (fig. S10, B, C, F, and G). Last, we tested whether differences in single-cell, pre-division NAD(H) levels could help explain activated CD4$^+$ T and B cell proliferative heterogeneity. Like CD8$^+$ T cells, higher pre-division NAD(P)H levels predicted faster rates through the cell cycle and the time to the first division (Fig. 4, J and K).

DISCUSSION

Heterogeneity underlies adaptive immune responses with responding clones varying in the number of divisions they undergo and the programs they adopt. Even the daughter cells of a single clone exhibit a range of proliferative and functional potential (*55*–*59*). Antigen receptor diversity determining a lymphocyte's affinity for a cognate antigen is understood to be a primary driver of these phenomena (*3*–*11*). Whereas the proximal signaling and downstream transcriptional responses that scale with affinity are well characterized, the biochemical responses to affinity and their downstream mechanisms are largely undefined. Here, we identify NAD biosynthesis as a central biochemical mediator of affinity-driven lymphocyte responses. Moreover, we find that cell-to-cell variation in this single pathway is sufficient to explain large facets of inter- and intraclonal heterogeneity.

In responding to naive lymphocytes, the strength of the activating signal determines the rate of quiescence exit and proliferation. Downstream of these mitogenic signals, cells are instructed to rewire their metabolism and meet the biochemical demands of rapid proliferation. The relationship among activating signal strength, cell cycle dynamics, and metabolic remodeling has been largely understood through the lens of signaling and gene regulation. Among these pathways, the most well-described are mTOR, Myc, and IRF4. All three factors are sensitive to the magnitude of TCR signaling, and each plays essential roles in patterning long-term proliferative and metabolic potential during early T cell activation (*8*, *11*, *13*, *14*, *16*–*19*, *21*–*25*, *60*). Whereas IRF4 is dispensable during early activation, Myc expression and mTOR signaling are essential for T cell quiescence exit and the anabolic program necessary to sustain growth (*8*, *17*, *18*, *21*, *24*, *25*, *60*). In large part, mTOR and Myc support T cell expansion and differentiation through their regulation of a broad range of key metabolic processes such as glucose import, amino acid uptake, and mitochondrial remodeling during the early stages of activation (*1*, *12*, *15*, *16*, *18*, *21*–*23*, *25*). Given that these anabolic mediators are tuned by antigen receptor signaling, we hypothesized that specific metabolic pathways would likewise be sensitive to the strength of the activation signal.

Through unbiased metabolomics analysis on OT-I T cells stimulated with peptides of varying affinity, we identified NAD biosynthesis as a central node of affinity-dependent metabolic changes during early activation. Whereas NAD biosynthesis is understood to be required in activated T cells and can function as a marker of resting versus activated cells, the specific cellular functions supported by it and its connection to affinity-dependent biology were previously unexplored. Using an in vitro system to manipulate cellular NAD levels, we identified the NAD salvage pathway as a mediator of quiescence exit and proliferation rates downstream of TCR stimulation. Collectively, our data indicate that the NAD salvage pathway regulates a quiescence checkpoint in naive lymphocytes. Accompanying this NAD-dependent cell cycle entry, we observed a recovery in Myc protein expression and mTOR signaling. This suggests that these critical anabolic pathways are not only upstream of lymphocyte metabolic rewiring but also that their sustained activity requires positive feedback from the successful deployment of this new biochemical program. Mechanistically, we found that NAD biosynthesis sets the rate of cell cycle entry through the control of GAPDH activity and central carbon metabolism downstream, as well as a majority of activation-dependent metabolic changes. Thus, NAD biosynthesis functions as a metabolic hub that scales with TCR signal strength to orchestrate the broader affinity-dependent metabolism and cell biology of T cell activation.

Whereas affinity is a primary determinant of interclonal lymphocyte dynamics, substantial heterogeneity remains within single-clonal lineages. This has largely been explained through the action of extrinsic factors, such as cytokines, and through processes including asymmetric division. Asymmetric inheritance of factors and pathways, such as Myc, mTOR, PI3K signaling, and the proteasome, has been shown to generate metabolic heterogeneity within a clonal lineage at the time of the first division (*18*, *22*, *61*–*63*). Given that we observed single-cell differences in NAD(P)H autofluorescence before the first division and that NAD biosynthesis capacity regulates subsequent proliferation rates, we asked whether NAD(P)H autofluorescence is similarly deterministic of future cell behavior.

We found that within a population of identically stimulated cells, NADH levels predicted proliferation rates, metabolic activity, the kinetics of effector function acquisition, and persistence after the contraction phase of an acute infection. Moreover, we found that across populations of disparately stimulated cells, selecting cells with similar NADH levels normalized the rate of quiescence exit and proliferation. Like $CD8^+$ T cells, we found a similar role for NAD biosynthesis and single-cell variance in $CD4^+$ T cells and B cells, suggesting a broader phenomenon in lymphocytes. Together, these findings highlight how early differences in cellular metabolism play a crucial role in dictating lymphocyte heterogeneity, through mechanisms that precede what has been previously described in the context of asymmetric division.

Combined, our data support a model in which NAD biosynthesis scales with the strength of mitogenic signaling to license the metabolic remodeling required for cell cycle entry and early proliferation. Our data suggest that NAD salvage pathway activity, rather than precursor availability, is rate limiting for lymphocyte NAD production and thereby function. In this manner, cells with lower NAD(H) levels are biochemically constrained and unable to quickly exit quiescence relative to cells that generate more NAD. In populations receiving a low- versus high-affinity stimulus, there are high-affinity cells that are limited by lower NAD biosynthesis and lower-affinity cells that maximally generate NAD for their given stimulation strength. This metabolic constraint is therefore sufficient to normalize proliferative behavior between these two groups despite differences in the initial mitogenic signal. Combined, we believe that this model helps explain why cell-to-cell NAD(H) variation underlies large facets of inter- and intraclonal heterogeneity.

These findings provide a metabolic framework for how ligand affinity and signal strength dictate clonal lymphocyte dynamics. We believe that this offers a comprehensive model for how mitogenic signaling coordinates cell cycle progression via a single metabolite. Our data illustrate how canonical signaling networks must work in concert with metabolic reprogramming to ensure that a newly deployed cellular program can be supported by a cell's biochemical state. Thus, whereas signaling sets the limits of cellular function, single-cell differences in metabolism govern their behavior. This paradigm suggests that other aspects of cellular metabolism might similarly contribute to heterogeneity in other developmental processes and might be leveraged to rapidly identify cells with desired functional properties for cellular engineering or cell-based therapies.

MATERIALS AND METHODS

Study design

The major goal of this study was to identify the metabolic processes that facilitate affinity-dependent cell biology downstream of antigen receptor signaling and determine whether this underlies inter- and intraclonal heterogeneity found during lymphocyte responses. To this end, we performed unbiased mass spectrometry to identify NAD biosynthesis as a central metabolic mediator of T cell affinity–dependent biology. We substantiated this using in vivo genetic tools and in vitro manipulation of NAD biosynthesis to dissect the cell biology and molecular mechanisms underlying this. We then used a NAD(P)H sorting strategy to formally evaluate the role of single-cell variation in this pathway on lymphocyte proliferative and functional heterogeneity.

Mice

Sex-matched male and female C57BL/6 (Jax #000664), OT-I (Jax #003831), CD8-Cre (Jax #008766), B6-Ly5.1 (Jax #002014), and Myc-GFP (Jax #019075) mice (6 to 8 weeks old) were purchased from Jackson Laboratories and maintained in house. Namptfl/fl and $Nampt^{Tg}$ mice were provided by J. Baur (*50*, *54*). P14 (JAX: Tg(TcrLCMV)327Sdz) animals were a gift from E. John Wherry. Spleens from Nur77-GFP mice were a gift from B. Au Yeung (*64*). All mice were housed under specific pathogen–free conditions with a 12-hour on/off light cycle at the Children's Hospital of Philadelphia. All experiments were performed in accordance with the Institutional Animal Care and Use Committee of the Children's Hospital of Philadelphia (IAC 21-001325).

Lymphocyte cell culture

Murine $CD8^+$ T cells, $CD4^+$ T cells, or B cells were isolated from the spleen and lymph nodes by negative selection using an EasySep Mouse Isolation kit (StemCell Technologies). Human T cells were obtained from the University of Pennsylvania Human Immunology Core. Unless otherwise noted, OT-I T cells were stimulated with SIINFEKL (1 μg/ml; N4), SIIQFEKL (Q4), SIITFEKL (T4), or SIIGFEKL (G4) peptides (Anaspec), anti-CD28 (clone 37.51, BioLegend), and rIL-2 (BioLegend). P14 T cells were activated as OT-I T cells, using GP33 (KAVYNFATC) peptide (GenScript). C57BL/6 $CD8^+$ T and $CD4^+$ T cells were stimulated with anti-CD3ε (clone 145-2C11, BioLegend), anti-CD28, and rIL-2 (BioLegend). Human T cells were stimulated with anti-CD3ε (clone OKT3, BioLegend) and rIL-2 (Biolegend). B cells were stimulated with anti-IgM (Goat anti-mouse, Jackson Immunoresearch), CD40 (Clone FGK 4.5, BioXcell), or LPS (Sigma-Aldrich).

For all experiments using drug or metabolite supplementation, the following doses were used, unless otherwise noted: 100 nM FK866 (Daporinad), 100 μM NR (Elysium), tryptophan (Sigma-Aldrich), NA (Sigma-Aldrich), 1 μM rotenone (Sigma-Aldrich), 1 μM oligomycin (Sigma-Aldrich), 10 mM 2-deoxy-D-glucose, 0.2 mM FCCP (Sigma-Aldrich), 10 μM rucaparib (MedChemExpress), 50 μM EX527 (Selleck), and 65 μM 78c (Tocris).

Flow cytometry

All flow cytometry was performed on a CytoFLEX LX or CytoFLEX S cytometer (Beckman Coulter). Data were analyzed using FlowJo software (Treestar). Cell division was measured by labeling cells with CellTrace Violet or CellTrace Yellow (Invitrogen) before activation and evaluated for proliferation at the indicated time points. Staining was performed with combinations of the following antibodies: anti-CD8 (1:300; clone 53-6.7, Thermo Fisher Scientific), $TCR\beta^+$ (1:300; clone H57-597, Thermo Fisher Scientific), $CD44^+$ (1:300; IM7, Thermo Fisher Scientific), Ki-67 (1:600; SolA15, Thermo Fisher Scientific), anti-cMyc (1:400; D84C12, Cell Signaling Technology), anti-S6 (1:75; 54D2, Cell Signaling Technology), and anti–phospho-S6 (1:75; D57.2.2E, Cell Signaling Technology). DNA content was measured by DAPI. Viability was assessed using eBioscience Fixable Viability Dye eFluor 780 was used (Thermo Fisher Scientific). NAD(P)H autofluorescence was determined by signal excited from the ultraviolet laser (375 nm) and detected at 450 nm. Triplicate sample wells were run asynchronously to control for fluctuations in the autofluorescence signal. The absolute cell number in each sample was back-calculated from recorded cytometer sample volumes after calibration. Cytokine was measured by adding

brefeldin A (Invivogen) 30 min after the addition of PMA (20 ng/ml; Thermo Fisher Scientific) and ionomycin (20 ng/ml, Cayman); 4.5 hours after restimulation, cells were fixed, permeabilized, and stained with anti–IFN-γ (1:100; XMG1.2, Thermo Fisher Scientific), anti–TNF-α (1:100; MP6-XT22, Thermo Fisher Scientific), and anti-IL-2 (1:100; MQ1-17H12, Thermo Fisher Scientific). Tetramer staining was performed with SIINFEKL-loaded H2-Kb tetramer (NIH tetramer core) for 1 hour at 4°C before surface staining. The geometric MFI (gMFI) was calculated and normalized to TCRβ gMFI to calculate relative affinity.

Flow cytometric cell sorting

Cell sorting of T cells and B cells was done on a Cytek Aurora CS cell sorter. For compensation calculation, FK866-treated CD8 T cells were used as a negative control for NAD(P)H autofluorescence. During the sort, the chamber was kept at 37°C. To normalize NAD(P)H levels across N4 and G4/T4 populations, cells were analyzed together to generate gates and determine frequencies of NAD(P)H-high and -low cells. To distinguish populations of differentially stimulated cells, cells were stained with either high or low CTY concentrations and sorted separately (Fig. 4F) or using 45.1/2 congenic markers and mixed before sorting (fig. S9D).

Seahorse analysis

Analysis was performed on cells at the noted time points postactivation. Cells were plated at 1×10^5 cells per well in a 96-well Seahorse assay plate, pretreated with Cell-Tak (Corning). Cells were equilibrated to 37°C for 30 min before assay. OCR (in pmol/min) and ECAR (in mpH/min) were measured as indicated upon cell treatment with oligomycin (1.5 μM, Cayman), FCCP (1.5 μM, Cayman) or Bam15 (2.5 μM, Cayman), rotenone (1 μM, Cayman), and antimycin A (1 μM, Sigma-Aldrich) according to the manufacturer's instructions.

L. monocytogenes infection

Transgenic *L. monocytogenes* expressing ovalbumin (Lm-Ova) was a gift from H. Shen. For infection, Lm-Ova was grown to early log phase (OD600 nm of 0.1) in brain-heart infusion medium (Becton Dickinson), washed and diluted with sterile saline, and then inoculated intravenously (10^4 colony-forming units per mouse).

qPCR

RNA was extracted using the Zymo Quick-RNA MicroPrep Kit without DNase I treatment according to the manufacturer's protocol. One microgram of total RNA was reverse-transcribed into cDNA using Thermo Maxima H Minus Reverse Transcriptase, 100 U per 20 μl reaction with 25 pmol each oligo$(dT)_{18}$ and random hexamer primers. RT reaction was incubated for 10 min at 25°C, 15 min at 50°C, and then terminated by heating for 5 min at 85°C. cDNA was diluted 1:10 before being used in reverse transcription quantitative polymerase chain reaction (RT-qPCR) with PowerTrack SYBR Green Master Mix on a Bio-Rad CFX384 real-time qPCR system. Nampt primers: forward, ACCAATGGCCTTGGGGTTAATG; reverse, TCCCCGCTGGTGTCCTATGT. Technical triplicates were quantified using 2-ΔCt normalized to Pol2Ra.

Western blot

Two million cells were lysed in ice-cold buffer containing 50 mM tris (pH 8.0), 1 mM EDTA, 150 mM NaCl, 1% NP-40, 0.5% Na deoxycholate, and 0.1% SDS, 10 mM NaF, 1 mM Na3VO4, and proteinase inhibitor cocktail (Roche, no. 11836170001). Samples were separated by SDS-PAGE, followed by transfer using the Trans-Blot Turbo Transfer System. Membranes were blocked with 5% dry nonfat dairy milk in tris-buffered saline with Tween 20 (TBS-T; 0.1%) for 30 to 60 min. Primary antibodies were incubated in TBS + 1% Casein overnight at 4°C with shaking. Three to five washes for 3 to 10 min were performed before secondary antibodies were incubated in 5% milk in TBS-T for 30 to 60 min at room temperature with rocking. Washes were performed before membranes were visualized using SuperSignal West Pico PLUS or Femto Chemiluminescent Substrate and the ChemiDoc MP Imaging System. Antibodies used NAMPT (1:1000; A300-372A, Bethyl Laboratories), pS6 (1:5000; D57.2.2E $Ser^{235/236}$, Cell Signaling Technology), S6 (1:5000; 5G10, Cell Signaling Technology), pS6K (1:1000; 108D2, Cell Signaling Technology), S6K (1:1000; 49D7, Cell Signaling Technology), and anti-actin hFAB rhodamine (1:2000; Bio-Rad).

NAD enzymatic cycling assay

Cells were washed with PBS, pelleted, and flash-frozen. Lysates were prepared with 0.6 M perchloric acid at 4°C. Cleared acid extracts were collected after pelleting insoluble material at 4°C. NAD standards (4 μl) or diluted tissue acid extracts were combined with 100 μl of cycling reaction reagent: 2% ethanol, alcohol dehydrogenase (100 μg/ml), diaphorase (10 μg/ml), 20 μM resazurin, 10 μM flavin mononucleotide, 10 mM nicotinamide, and 0.1% BSA in 100 mM phosphate buffer (pH 8.0). After 20 to 30 min, resorufin accumulation was measured with excitation at 544 nm and emission at 590 nm.

NADH FLIM

NADH FLIM was performed on an LSM 710 (Zeiss) using a femtosecond-pulsed two-photon laser (Coherent) as described (*65*). Briefly, cells were mounted on the microscope in a four-compartment CELLview cell culture dish with a thin glass bottom (catalog #627870, Greiner) in 500 μl of Tyrodes solution, with temperature maintained at 37°C. NADH was excited at 730 nm (<5 mW on the sample, 1-min acquisition time), and the autofluorescence was detected through a 680-nm short-pass and 460/50-nm bandpass emission filter. Time-correlated single-photon counting was performed using an HPM-100-40 detector and the SPCM 9.81 software (both Becker and Hickl). FLIM images were analyzed by SPCImage 8.0 using a biexponential decay with T1 and T2 being fixed to 400 and 2500 ps for free and protein-bound NADH. The fixed lifetime components were used to reduce the number of photons required for a valid lifetime calculation. Nuclear NADH was quantified using regions of interest (ROIs), averaging a minimum of five cells per image section. Mitochondrial NADH was quantified using the threshold function of SPCImage and verified using ROIs for individual conditions.

Statistical analysis

Representative data are shown from experiments that were repeated at least three times. Each data point plotted is the mean of at least three replicates per well with error bars representing the SD. The sample size and number of independent experiments are indicated in the figure captions. All statistical tests are described in the figure captions and were performed in Prism (GraphPad). No data were excluded. *P* values of 0.05 or less were considered statistically significant.

Supplementary Materials

This PDF file includes:
Materials and Methods
Figs. S1 to S10
Tables S1 and S2

Other Supplementary Material for this manuscript includes the following:
Data files S1 and S2
MDAR Reproducibility Checklist

REFERENCES AND NOTES

1. N. M. Chapman, M. R. Boothby, H. Chi, Metabolic coordination of T cell quiescence and activation. *Nat. Rev. Immunol.* **20**, 55–70 (2020).
2. R. I. K. Geltink, R. L. Kyle, E. L. Pearce, Unraveling the complex interplay between T cell metabolism and function. *Annu. Rev. Immunol.* **36**, 461–488 (2018).
3. S. Heinzel, J. M. Marchingo, M. B. Horton, P. D. Hodgkin, The regulation of lymphocyte activation and proliferation. *Curr. Opin. Immunol.* **51**, 32–38 (2018).
4. K. A. Allison, E. Sajti, J. G. Collier, D. Gosselin, T. D. Troutman, E. L. Stone, S. M. Hedrick, C. K. Glass, Affinity and dose of TCR engagement yield proportional enhancer and gene activity in CD4+ T cells. *eLife* **5**, e10134 (2016).
5. J. M. Conley, M. P. Gallagher, A. Rao, L. J. Berg, Activation of the Tec kinase ITK controls graded IRF4 expression in response to variations in TCR signal strength. *J. Immunol.* **205**, 335–345 (2020).
6. M. P. Gallagher, J. M. Conley, P. Vangala, M. Garber, A. Reboldi, L. J. Berg, Hierarchy of signaling thresholds downstream of the T cell receptor and the Tec kinase ITK. *Proc. Natl. Acad. Sci. U.S.A.* **118**, e2025825118 (2021).
7. A. V. Gett, F. Sallusto, A. Lanzavecchia, J. Geginat, T cell fitness determined by signal strength. *Nat. Immunol.* **4**, 355–360 (2003).
8. K. Man, M. Miasari, W. Shi, A. Xin, D. C. Henstridge, S. Preston, M. Pellegrini, G. T. Belz, G. K. Smyth, M. A. Febbraio, S. L. Nutt, A. Kallies, The transcription factor IRF4 is essential for TCR affinity-mediated metabolic programming and clonal expansion of T cells. *Nat. Immunol.* **14**, 1155–1165 (2013).
9. D. A. Price, J. M. Brenchley, L. E. Ruff, M. R. Betts, B. J. Hill, M. Roederer, R. A. Koup, S. A. Migueles, E. Gostick, L. Wooldridge, A. K. Sewell, M. Connors, D. C. Douek, Avidity for antigen shapes clonal dominance in CD8+ T cell populations specific for persistent DNA viruses. *J. Exp. Med.* **202**, 1349–1361 (2005).
10. A. C. Richard, A. T. L. Lun, W. W. Y. Lau, B. Göttgens, J. C. Marioni, G. M. Griffiths, T cell cytolytic capacity is independent of initial stimulation strength. *Nat. Immunol.* **19**, 849–858 (2018).
11. S. Solouki, W. Huang, J. Elmore, C. Limper, F. Huang, A. August, TCR signal strength and antigen affinity regulate CD8(+) memory T cells. *J. Immunol.* **205**, 1217–1227 (2020).
12. D. K. Finlay, E. Rosenzweig, L. V. Sinclair, C. Feijoo-Carnero, J. L. Hukelmann, J. Rolf, A. A. Panteleyev, K. Okkenhaug, D. A. Cantrell, PDK1 regulation of mTOR and hypoxia-inducible factor 1 integrate metabolism and migration of CD8+ T cells. *J. Exp. Med.* **209**, 2441–2453 (2012).
13. C. S. Guy, K. M. Vignali, J. Temirov, M. L. Bettini, A. E. Overacre, M. Smeltzer, H. Zhang, J. B. Huppa, Y. H. Tsai, C. Lobry, J. Xie, P. J. Dempsey, H. C. Crawford, I. Aifantis, M. M. Davis, D. A. A. Vignali, Distinct TCR signaling pathways drive proliferation and cytokine production in T cells. *Nat. Immunol.* **14**, 262–270 (2013).
14. S. Heinzel, T. Binh Giang, A. Kan, J. M. Marchingo, B. K. Lye, L. M. Corcoran, P. D. Hodgkin, A Myc-dependent division timer complements a cell-death timer to regulate T cell and B cell responses. *Nat. Immunol.* **18**, 96–103 (2017).
15. J. L. Hukelmann, K. E. Anderson, L. V. Sinclair, K. M. Grzes, A. B. Murillo, P. T. Hawkins, L. R. Stephens, A. I. Lamond, D. A. Cantrell, The cytotoxic T cell proteome and its shaping by the kinase mTOR. *Nat. Immunol.* **17**, 104–112 (2016).
16. J. M. Marchingo, L. V. Sinclair, A. J. Howden, D. A. Cantrell, Quantitative analysis of how myc controls T cell proteomes and metabolic pathways during T cell activation. *eLife* **9**, e53725 (2020).
17. K. N. Pollizzi, C. H. Patel, I.-H. Sun, M.-H. Oh, A. T. Waickman, J. Wen, G. M. Delgoffe, J. D. Powell, mTORC1 and mTORC2 selectively regulate CD8(+) T cell differentiation. *J. Clin. Invest.* **125**, 2090–2108 (2015).
18. K. N. Pollizzi, I.-H. Sun, C. H. Patel, Y.-C. Lo, M.-H. Oh, A. T. Waickman, A. J. Tam, R. L. Blosser, J. Wen, G. M. Delgoffe, J. D. Powell, Asymmetric inheritance of mTORC1 kinase activity during division dictates CD8(+) T cell differentiation. *Nat. Immunol.* **17**, 704–711 (2016).
19. G. C. Preston, L. V. Sinclair, A. Kaskar, J. L. Hukelmann, M. N. Navarro, I. Ferrero, H. R. MacDonald, V. H. Cowling, D. A. Cantrell, Single cell tuning of Myc expression by antigen receptor signal strength and interleukin-2 in T lymphocytes. *EMBO J.* **34**, 2008–2024 (2015).
20. N. Ron-Harel, D. Santos, J. M. Ghergurovich, P. T. Sage, A. Reddy, S. B. Lovitch, N. Dephoure, F. K. Satterstrom, M. Sheffer, J. B. Spinelli, S. Gygi, J. D. Rabinowitz, A. H. Sharpe, M. C. Haigis, Mitochondrial biogenesis and proteome remodeling promote one-carbon metabolism for T cell activation. *Cell Metab.* **24**, 104–117 (2016).
21. H. Tan, K. Yang, Y. Li, T. I. Shaw, Y. Wang, D. B. Blanco, X. Wang, J. H. Cho, H. Wang, S. Rankin, C. Guy, J. Peng, H. Chi, Integrative proteomics and phosphoproteomics profiling reveals dynamic signaling networks and bioenergetics pathways underlying T cell activation. *Immunity* **46**, 488–503 (2017).
22. K. C. Verbist, C. S. Guy, S. Milasta, S. Liedmann, M. M. Kamiński, R. Wang, D. R. Green, Metabolic maintenance of cell asymmetry following division in activated T lymphocytes. *Nature* **532**, 389–393 (2016).
23. R. Wang, C. P. Dillon, L. Z. Shi, S. Milasta, R. Carter, D. Finkelstein, L. L. McCormick, P. Fitzgerald, H. Chi, J. Munger, D. R. Green, The transcription factor Myc controls metabolic reprogramming upon T lymphocyte activation. *Immunity* **35**, 871–882 (2011).
24. K. Yang, G. Neale, D. R. Green, W. He, H. Chi, The tumor suppressor Tsc1 enforces quiescence of naive T cells to promote immune homeostasis and function. *Nat. Immunol.* **12**, 888–897 (2011).
25. K. Yang, S. Shrestha, H. Zeng, P. W. F. Karmaus, G. Neale, P. Vogel, D. A. Guertin, R. F. Lamb, H. Chi, T cell exit from quiescence and differentiation into Th2 cells depend on Raptor-mTORC1-mediated metabolic reprogramming. *Immunity* **39**, 1056–1043 (2013).
26. L. V. Sinclair, A. J. Howden, A. Brenes, L. Spinelli, J. L. Hukelmann, A. N. Macintyre, X. Liu, S. Thomson, P. M. Taylor, J. C. Rathmell, J. W. Locasale, A. I. Lamond, D. A. Cantrell, Antigen receptor control of methionine metabolism in T cells. *eLife* **8**, e44210 (2019).
27. L. V. Sinclair, J. Rolf, E. Emslie, Y.-B. Shi, P. M. Taylor, D. A. Cantrell, Control of amino-acid transport by antigen receptors coordinates the metabolic reprogramming essential for T cell differentiation. *Nat. Immunol.* **14**, 500–508 (2013).
28. M. Nakaya, Y. Xiao, X. Zhou, J.-H. Chang, M. Chang, X. Cheng, M. Blonska, X. Lin, S.-C. Sun, Inflammatory T cell responses rely on amino acid transporter ASCT2 facilitation of glutamine uptake and mTORC1 kinase activation. *Immunity* **40**, 692–705 (2014).
29. J. C. Rathmell, C. J. Fox, D. R. Plas, P. S. Hammerman, R. M. Cinalli, C. B. Thompson, Akt-directed glucose metabolism can prevent Bax conformation change and promote growth factor-independent survival. *Mol. Cell. Biol.* **23**, 7315–7328 (2003).
30. F. R. Carbone, S. J. Sterry, J. Butler, S. Rodda, M. W. Moore, T cell receptor alpha-chain pairing determines the specificity of residue 262 within the Kb-restricted, ovalbumin257-264 determinant. *Int. Immunol.* **4**, 861–867 (1992).
31. S. C. Jameson, F. R. Carbone, M. J. Bevan, Clone-specific T cell receptor antagonists of major histocompatibility complex class I-restricted cytotoxic T cells. *J. Exp. Med.* **177**, 1541–1550 (1993).
32. K. A. Hogquist, S. C. Jameson, W. R. Heath, J. L. Howard, M. J. Bevan, F. R. Carbone, T cell receptor antagonist peptides induce positive selection. *Cell* **76**, 17–27 (1994).
33. C. Rosette, G. Werlen, M. A. Daniels, P. O. Holman, S. M. Alam, P. J. Travers, N. R. Gascoigne, E. Palmer, S. C. Jameson, The impact of duration versus extent of TCR occupancy on T cell activation: A revision of the kinetic proofreading model. *Immunity* **15**, 59–70 (2001).
34. M. A. Daniels, E. Teixeiro, J. Gill, B. Hausmann, D. Roubaty, K. Holmberg, G. Werlen, G. A. Holländer, N. R. Gascoigne, E. Palmer, Thymic selection threshold defined by compartmentalization of Ras/MAPK signalling. *Nature* **444**, 724–729 (2006).
35. J. D. Rabinowitz, C. Beeson, C. Wülfing, K. Tate, P. M. Allen, M. M. Davis, H. M. McConnell, Altered T cell receptor ligands trigger a subset of early T cell signals. *Immunity* **5**, 125–135 (1996).
36. N. Auphan-Anezin, G. Verdeil, A.-M. Schmitt-Verhulst, Distinct thresholds for CD8 T cell activation lead to functional heterogeneity: CD8 T cell priming can occur independently of cell division. *J. Immunol.* **170**, 2442–2448 (2003).
37. L. Malherbe, C. Hausl, L. Teyton, M. G. McHeyzer-Williams, Clonal selection of helper T cells is determined by an affinity threshold with no further skewing of TCR binding properties. *Immunity* **21**, 669–679 (2004).
38. A. E. Denton, R. Wesselingh, S. Gras, C. Guillonneau, M. R. Olson, J. D. Mintern, W. Zeng, D. C. Jackson, J. Rossjohn, P. D. Hodgkin, P. C. Doherty, S. J. Turner, Affinity thresholds for naive CD8+ CTL activation by peptides and engineered influenza A viruses. *J. Immunol.* **187**, 5733–5744 (2011).
39. C.-H. Chang, J. D. Curtis, L. B. Maggi Jr., B. Faubert, A. V. Villarino, D. O'Sullivan, S. C.-C. Huang, G. J. W. van der Windt, J. Blagih, J. Qiu, J. D. Weber, E. J. Pearce, R. G. Jones, E. L. Pearce, Posttranscriptional control of T cell effector function by aerobic glycolysis. *Cell* **153**, 1239–1251 (2013).
40. R. Geiger, J. C. Rieckmann, T. Wolf, C. Basso, Y. Feng, T. Fuhrer, M. Kogadeeva, P. Picotti, F. Meissner, M. Mann, N. Zamboni, F. Sallusto, A. Lanzavecchia, L-Arginine modulates T cell metabolism and enhances survival and anti-tumor activity. *Cell* **167**, 829–842.e13 (2016).
41. E. H. Ma, M. J. Verway, R. M. Johnson, D. G. Roy, M. Steadman, S. Hayes, K. S. Williams, R. D. Sheldon, B. Samborska, P. A. Kosinski, H. Kim, T. Griss, B. Faubert, S. A. Condotta, C. M. Krawczyk, R. J. DeBerardinis, K. M. Stewart, M. J. Richer, V. Chubukov, T. P. Roddy, R. G. Jones, Metabolic profiling using stable isotope tracing reveals distinct patterns of glucose utilization by physiologically activated CD8(+) T cells. *Immunity* **51**, 856–870.e5 (2019).

42. N. Ron-Harel, J. M. Ghergurovich, G. Notarangelo, M. W. LaFleur, Y. Tsubosaka, A. H. Sharpe, J. D. Rabinowitz, M. C. Haigis, T cell activation depends on extracellular alanine. *Cell Rep.* **28**, 3011–3021.e4 (2019).
43. J. Edwards-Hicks, M. Mitterer, E. L. Pearce, J. M. Buescher, Metabolic dynamics of in vitro CD8+ T cell activation. *Metabolites* **11**, 12 (2020).
44. W. Bailis, J. A. Shyer, J. Zhao, J. C. G. Canaveras, F. J. al Khazal, R. Qu, H. R. Steach, P. Bielecki, O. Khan, R. Jackson, Y. Kluger, L. J. Maher III, J. Rabinowitz, J. Craft, R. A. Flavell, Distinct modes of mitochondrial metabolism uncouple T cell differentiation and function. *Nature* **571**, 403–407 (2019).
45. E. Katsyuba, J. Auwerx, Modulating NAD(+) metabolism, from bench to bedside. *EMBO J.* **36**, 2670–2683 (2017).
46. S. Bruzzone, F. Fruscione, S. Morando, T. Ferrando, A. Poggi, A. Garuti, A. D'Urso, M. Selmo, F. Benvenuto, M. Cea, G. Zoppoli, E. Moran, D. Soncini, A. Ballestrero, B. Sordat, F. Patrone, R. Mostoslavsky, A. Uccelli, A. Nencioni, Catastrophic NAD+ depletion in activated T lymphocytes through Nampt inhibition reduces demyelination and disability in EAE. *PLOS ONE* **4**, e7897 (2009).
47. Y. Wang, F. Wang, L. Wang, S. Qiu, Y. Yao, C. Yan, X. Xiong, X. Chen, Q. Ji, J. Cao, G. Gao, D. Li, L. Zhang, Z. Guo, R. Wang, H. Wang, G. Fan, NAD(+) supplement potentiates tumor-killing function by rescuing defective TUB-mediated NAMPT transcription in tumor-infiltrated T cells. *Cell Rep.* **36**, 109516 (2021).
48. J. Yoshino, J. A. Baur, S. I. Imai, NAD(+) intermediates: The biology and therapeutic potential of NMN and NR. *Cell Metab.* **27**, 513–528 (2018).
49. M. L. Chapman, M. R. Zaun, R. W. Gracy, Changes in NAD levels in human lymphocytes and fibroblasts during aging and in premature aging syndromes. *Mech. Ageing Dev.* **21**, 157–167 (1983).
50. A. Rongvaux, M. Galli, S. Denanglaire, F. van Gool, P. L. Drèze, C. Szpirer, F. Bureau, F. Andris, O. Leo, Nicotinamide phosphoribosyl transferase/pre-B cell colony-enhancing factor/visfatin is required for lymphocyte development and cellular resistance to genotoxic stress. *J. Immunol.* **181**, 4685–4695 (2008).
51. W. J. Quinn III, J. Jiao, T. TeSlaa, J. Stadanlick, Z. Wang, L. Wang, T. Akimova, A. Angelin, P. M. Schäfer, M. D. Cully, C. Perry, P. K. Kopinski, L. Guo, I. A. Blair, L. R. Ghanem, M. S. Leibowitz, W. W. Hancock, E. K. Moon, M. H. Levine, E. B. Eruslanov, D. C. Wallace, J. A. Baur, U. H. Beier, Lactate limits T cell proliferation via the NAD(H) redox state. *Cell Rep.* **33**, 108500 (2020).
52. J. M. Drijvers, J. E. Gillis, T. Muijlwijk, T. H. Nguyen, E. F. Gaudiano, I. S. Harris, M. W. LaFleur, A. E. Ringel, C.-H. Yao, K. Kurmi, V. R. Juneja, J. D. Trombley, M. C. Haigis, A. H. Sharpe, Pharmacologic screening identifies metabolic vulnerabilities of $CD8^+$ T cells. *Cancer Immunol. Res.* **9**, 184–199 (2021).
53. R. R. Gerner, S. Macheiner, S. Reider, K. Siegmund, F. Grabherr, L. Mayr, B. Texler, P. Moser, M. Effenberger, H. Schwaighofer, A. R. Moschen, B. Kircher, H. Oberacher, R. Zeiser, H. Tilg, D. Nachbaur, Targeting NAD immunometabolism limits severe graft-versus-host disease and has potent antileukemic activity. *Leukemia* **34**, 1885–1897 (2020).
54. D. W. Frederick, J. G. Davis, A. Dávila Jr., B. Agarwal, S. Michan, M. A. Puchowicz, E. Nakamaru-Ogiso, J. A. Baur, Increasing NAD synthesis in muscle via nicotinamide phosphoribosyltransferase is not sufficient to promote oxidative metabolism. *J. Biol. Chem.* **290**, 1546–1558 (2015).
55. J. Arsenio, B. Kakaradov, P. J. Metz, S. H. Kim, G. W. Yeo, J. T. Chang, Early specification of CD8+ T lymphocyte fates during adaptive immunity revealed by single-cell gene-expression analyses. *Nat. Immunol.* **15**, 365–372 (2014).
56. V. R. Buchholz, M. Flossdorf, I. Hensel, L. Kretschmer, B. Weissbrich, P. Gräf, A. Verschoor, M. Schiemann, T. Höfer, D. H. Busch, Disparate individual fates compose robust CD8+ T cell immunity. *Science* **340**, 630–635 (2013).
57. J. T. Chang, V. R. Palanivel, I. Kinjyo, F. Schambach, A. M. Intlekofer, A. Banerjee, S. A. Longworth, K. E. Vinup, P. Mrass, J. Oliaro, N. Killeen, J. S. Orange, S. M. Russell, W. Weninger, S. L. Reiner, Asymmetric T lymphocyte division in the initiation of adaptive immune responses. *Science* **315**, 1687–1691 (2007).
58. C. Gerlach, J. C. Rohr, L. Perié, N. van Rooij, J. W. J. van Heijst, A. Velds, J. Urbanus, S. H. Naik, H. Jacobs, J. B. Beltman, R. J. de Boer, T. N. M. Schumacher, Heterogeneous differentiation patterns of individual CD8+ T cells. *Science* **340**, 635–639 (2013).
59. S. M. Kaech, W. Cui, Transcriptional control of effector and memory CD8+ T cell differentiation. *Nat. Rev. Immunol.* **12**, 749–761 (2012).
60. K. Araki, A. P. Turner, V. O. Shaffer, S. Gangappa, S. A. Keller, M. F. Bachmann, C. P. Larsen, R. Ahmed, mTOR regulates memory CD8 T-cell differentiation. *Nature* **460**, 108–112 (2009).
61. C. E. Widjaja, J. G. Olvera, P. J. Metz, A. T. Phan, J. N. Savas, G. de Bruin, Y. Leestemaker, C. R. Berkers, A. de Jong, B. I. Florea, K. Fisch, J. Lopez, S. H. Kim, D. A. Garcia, S. Searles, J. D. Bui, A. N. Chang, J. R. Yates III, A. W. Goldrath, H. S. Overkleeft, H. Ovaa, J. T. Chang, Proteasome activity regulates CD8+ T lymphocyte metabolism and fate specification. *J. Clin. Invest.* **127**, 3609–3623 (2017).
62. Y.-H. Chen, R. Kratchmarov, W.-H. W. Lin, N. J. Rothman, B. Yen, W. C. Adams, S. A. Nish, J. C. Rathmell, S. L. Reiner, Asymmetric PI3K activity in lymphocytes organized by a PI3K-mediated polarity pathway. *Cell Rep.* **22**, 860–868 (2018).
63. S. Liedmann, X. Liu, C. S. Guy, J. C. Crawford, D. A. Rodriguez, D. Kuzuoğlu-Öztürk, A. Guo, K. C. Verbist, J. Temirov, M. J. Chen, D. Ruggero, H. Zhang, P. G. Thomas, D. R. Green, Localization of a TORC1-eIF4F translation complex during CD8(+) T cell activation drives divergent cell fate. *Mol. Cell* **82**, 2401–2414.e9 (2022).
64. J. Zikherman, R. Parameswaran, A. Weiss, Endogenous antigen tunes the responsiveness of naive B cells but not T cells. *Nature* **489**, 160–164 (2012).
65. P. M. Schaefer, D. Hilpert, M. Niederschweiberer, L. Neuhauser, S. Kalinina, E. Calzia, A. Rueck, B. von Einem, C. A. F. von Arnim, Mitochondrial matrix pH as a decisive factor in neurometabolic imaging. *Neurophotonics* **4**, 045004 (2017).

Acknowledgments: We thank the Children's Hospital Flow Cytometry Core for providing support and instrumentation; W. J. Quinn 3rd for early discussions that inspired this work; J. Henao-Mejia, D. Allman, and A. Wells for feedback and thoughtful discussion; and all members of the Bailis laboratory for providing feedback and support. **Funding:** This work was supported by NIH grant K22AI141758 (to W.B.), NIH grant R35GM138085 (to W.B.), Children's Hospital of Philadelphia Cell and Gene Therapy Collaborative SEED Award (to W.B.), Children's Hospital of Philadelphia Junior Faculty Pilot Grant (to W.B.), NIH grant R01DK098656 (to J.A.B.), NIH grant R01HL165792 (to J.A.B.), NIH grant P30ES013508 (to C.M.), NIH R01AI165706 (to B.A.-Y.), NIH grant F31CA261156 (to L.T.), Transfusion Medicine Research Training Program 2T32HL00777528 (to E.C.), Microbial Pathogenesis and Genomics Training Grant 5T32AI141393 (to B.G.), and Immunobiology of Normal and Neoplastic Lymphocytes Training Grant T32CA009140 (to K.R.). **Author contributions:** Conceptualization: W.B. Methodology: L.T., C.Q., J.D., P.S., and C.M. Investigation: L.T., T.N.V.L., E.C., C.Q., K.T., J.D., P.S., J.N., J.X., B.G., E.H., K.R., M.S., and J.E. Formal analysis: M.K. Visualization: L.T. and M.K. Funding acquisition: W.B., J.A.B., C.M., B.A.-Y., and D.C.W. Supervision: W.B., J.A.B., and C.M. Writing—original draft: L.T. and W.B. Writing—review and editing: L.T., T.N.V.L., E.C., J.A.B., and W.B. **Competing interests:** J.A.B. reports receiving research funding and materials from the NIH, Pfizer, Elysium Health, and Metro International Biotech; and receiving consulting fees from Pfizer, Elysium Health, and Cytokinetics. J.A.B. holds a patent for using NAD precursors in liver injury (U.S. Patent No. 11,103,496 B2). W.B. and J.A.B. hold a provisional patent (U.S. Patent No. 63/582,577). The other authors declare that they have no competing interests. **Data and materials availability:** All mass spectrometry data have been deposited and made publicly available through MetaboLights, EBI (accession number: MTBLS9178). Tabulated data underlying the figures are available in data file S2. All other data needed to evaluate the conclusions in the paper are present in the paper or the Supplementary Materials.

Submitted 12 July 2023
Accepted 22 February 2024
Published 15 March 2024
10.1126/sciimmunol.adj7238